

Contents lists available at ScienceDirect

Journal of the Mechanics and Physics of Solids

journal homepage: www.elsevier.com/locate/jmps



Mechanics of bistable cross-shaped structures through loading-path controlled 3D assembly



Guoquan Luo^{a,b,c,1}, Haoran Fu^{a,d,1}, Xu Cheng^{a,b}, Ke Bai^{a,b}, Liping Shi^c, Xiaodong He^c, John A. Rogers^{e,f}, Yonggang Huang^{f,g}, Yihui Zhang^{a,b,*}

^a Applied Mechanics Laboratory, Department of Engineering Mechanics, Tsinghua University, Beijing 100084, PR China

^b Center for Flexible Electronics Technology, Tsinghua University, Beijing 100084, PR China

^c National Key Laboratory of Science and Technology on Advanced Composite in Special Environments, Harbin Institute of Technology, Harbin 150080, PR China

^d Institute of Flexible Electronics Technology of THU, Zhejiang, Jiaxing 314006, PR China

^e Departments of Materials Science and Engineering, Biomedical Engineering, Chemistry, Neurological Surgery, Mechanical Engineering, Electrical Engineering and Computer Science, Simpson Querrey Institute for Bio-Nanotechnology, Northwestern University, Evanston, IL 60208, United States

^f Center for Bio-Integrated Electronics, Northwestern University, Evanston, IL 60208, United States

^g Departments of Civil and Environmental Engineering, Mechanical Engineering and Materials Science and Engineering, Northwestern University, Evanston, IL 60208, United States

ARTICLE INFO

Article history:

Received 1 March 2019

Revised 24 April 2019

Accepted 12 May 2019

Available online 15 May 2019

Keywords:

Bistable structure

Loading path

3D assembly

Postbuckling

ABSTRACT

Morphable three-dimensional (3D) structures capable of reversible shape changes between distinct geometric configurations have widespread applications in many important engineering areas. Recent advances in mechanically-guided 3D assembly provided a powerful approach to achieve morphable 3D mesostructures in a broad set of high-performance materials, over length scales from several micrometers to tens of centimeters. This approach relies on prestrained elastomer substrates released with different sequences to trigger the stabilization of distinct 3D buckling modes in specially engineered 2D precursor structures. Many of the reported 2D precursor structures are constructed with ribbon components that incorporate creases with reduced stiffness at strategic locations. The design of crease geometries and crease locations is essential to the structural bistability through this loading-path approach, which requires the development of a theory to serve as the design basis. This paper presents a finite-deformation model to analyze the stability of different buckling modes induced during the simultaneous and sequential compressions of structures with cross-shaped ribbon geometries, a very representative class of precursor patterns. By introducing a perturbation method to obtain an analytic solution to the deformed configuration of a uniform beam, a theoretical model is developed to predict the postbuckling deformations in cross-shaped ribbon structures with a prescribed number of creases. Based on the analyses of the strain-energy landscape, a stability coefficient is proposed to evaluate the bistability of cross-shaped ribbon structures. The developed model is validated by finite element analyses (FEA) and experimental measurements of structures with a broad range of cross-shaped geometries. This model allows the construction of design diagrams to identify the bistability for a variety of geometric parameters, including the normalized width and location of each crease in the cross-shaped patterns.

* Corresponding author at: Applied Mechanics Laboratory, Department of Engineering Mechanics, Tsinghua University, Beijing 100084, PR China.

E-mail address: yihuizhang@tsinghua.edu.cn (Y. Zhang).

¹ These authors contributed equally to this work.

These results elucidate how to select the various design parameters to achieve bistable 3D structures through the loading-path approach. Furthermore, the developed model is extended to the bistability analyses of precursor structures with generalized cross patterns and cross-shaped patterns consisting of locally stiffened elements. This study offers a theoretical reference for the design of ribbon-shaped mesostructures to achieve diverse morphable microelectronic devices.

© 2019 Elsevier Ltd. All rights reserved.

1. Introduction

Morphable three-dimensional (3D) structures whose shapes can be changed and stabilized between different configurations on demand have important implications in many emerging engineering areas, from micro-electromechanical systems (Ou et al., 2013), to biomedical device (Bolaños Quiñones et al., 2018; Shim et al., 2012), to micro robots (Felton et al., 2014; Hu et al., 2018), and to metamaterials (Filipov et al., 2015; Lv et al., 2014; Overvelde, 2016; Schenk and Guest, 2013; Silverberg, 2014; Yang and Silverberg, 2017). A few classes of approaches have been developed to design and manufacture morphable 3D structures in different types of materials, including those relying on origami/kirigami designs (Babaee et al., 2016; Bolaños Quiñones et al., 2018; Castle, 2014; Sussman, 2016; Cui et al., 2018; Dudit et al., 2016; Filipov et al., 2016; Overvelde, 2016; Rogers et al., 2016; Sussman, 2015; Yan, 2016; Zhang, 2015; Huang, 2015), strategically patterned active materials (e.g., shape memory polymers (Cui et al., 2017; Felton et al., 2014; Guo et al., 2018; Wang et al., 2019; Zhang et al., 2017a), hydrogels (Gladman et al., 2016; Jeon et al., 2017; Shim et al., 2012; Zhang et al., 2018b)), and mechanically-guided assembly through multistable buckling (Fu et al., 2018). The last class of approaches is fully compatible with planar semiconductor technologies and processing techniques well established in the electronics industries, thereby offering a versatile applicability to almost any class of materials (including brittle inorganic semiconductors and piezoelectric ceramics), spanning length scales from micrometers to millimeters. In the framework of assembly approaches (Liu et al., 2019; Xu et al., 2015; Zhang, 2015; Zhang et al., 2017b) that exploit the compressive buckling as a means to realize the controlled 2D-to-3D transformation, our previous work (Fu et al., 2018) showed that prestrained elastomers released with different sequences can trigger the stabilization of multiple, distinct 3D buckling modes in specially engineered precursor structures. Fig. 1 (middle panel) shows a very representative precursor design, with a cross-shaped ribbon configuration that has a four-fold rotational symmetry. Here, the creases (in green color) with reduced stiffnesses were introduced to trap the structure into the Shape-II mode during the sequential release of the biaxial prestrain, noting that the geometry of the Shape-II mode is distinct from that of the Shape-I mode formed during the simultaneous prestrain release. Previous studies demonstrated that only the designs with sufficiently flexible creases can enable the stabilization of the Shape-II mode. Therefore, the design of crease geometries and crease locations is essential in the formation of bistable shapes through this loading-path strategy. The

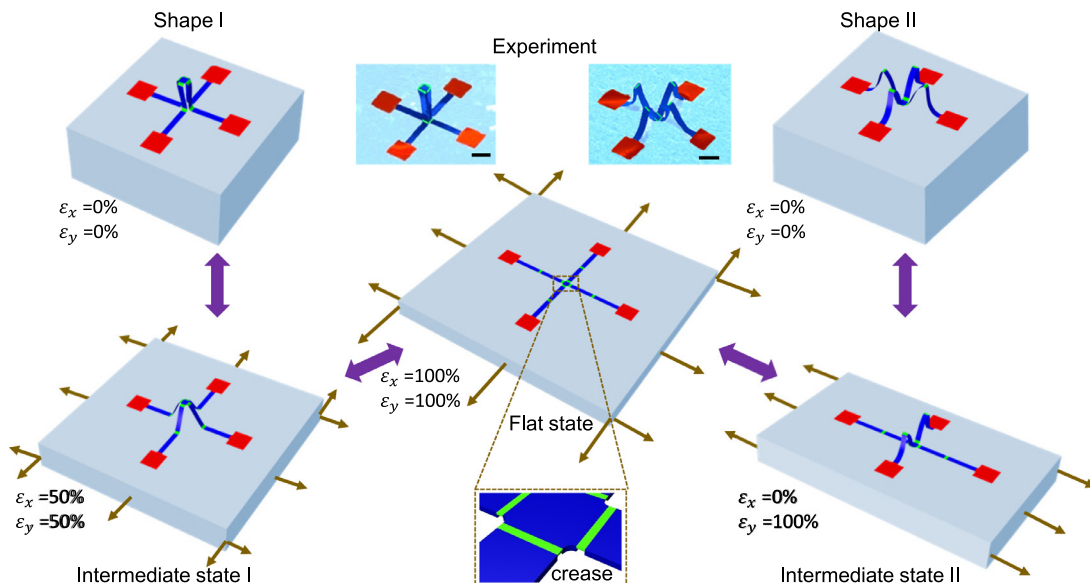


Fig. 1. Schematic illustration of a morphable 3D mesostructure realized through the loading-path controlled mechanical assembly. The middle top images are colorized SEM images, while the others are results of finite element analyses (FEA). Reprinted with permission from Fu et al. (2018), Copyright 2018, Macmillan Publishers Ltd.

previous studies mainly exploited iterative finite element analysis (FEA) as a basis of structural design, but this ‘trial and error’ process could be very cumbersome and time-consuming, since the designs usually involved many (e.g., > 5) independent geometric parameters. Hence, the widespread utility of the loading-path controlled assembly approach requires the development of a mechanics theory to provide general guidelines for rapid device design and optimization. Although remarkable progresses have been made in postbuckling theories of beams and films (Budiansky and Hutchinson, 1966; Chen et al., 2017; Dias and Audoly, 2015; Fu et al., 2019; Hui, 1988; Ni and Soh, 2014; Pan et al., 2017; Pan et al., 2014; Reis, 2015; Su et al., 2012; Xu and Potier-Ferry, 2016), either by energy minimization approaches (Chen et al., 2016a, 2013, 2016b; Jiang et al., 2007, 2008; Jiao et al., 2017; Liu et al., 2016; Song et al., 2009; Wang et al., 2015) or linear perturbation methods (Fan et al., 2017, 2018; Lacarbonara, 2008; Su et al., 2012), most of these studies focused on straight beams (Chen et al., 2013, 2016a, 2016b; Jiang et al., 2007, 2008; Jiao et al., 2017; Lacarbonara, 2008; Li et al., 2012, 2013; Miller et al., 2015; Song et al., 2009; Wagner and Vella, 2013; Wang et al., 2017) or curvy beams (Bian et al., 2017; Fan et al., 2018, 2017; Liu and Lu, 2016; Liu et al., 2016; Ma et al., 2016; Pan et al., 2017; Widlund et al., 2014; Yang et al., 2016) with uniform cross sections. Very few works were reported to investigate the postbuckling of beam/ribbon structures with non-uniform cross sections, such as the beam with a continuously changing cross section (Lacarbonara, 2008) or the beam with a stepwise variation in the cross section (Lacarbonara, 2008; Zhang et al., 2018a). It is noteworthy that the existing theories are not readily applicable to the bistability analyses of non-uniform beam/ribbon structures, as demanded in the loading-path controlled assembly approach.

The aim of this study is to present a systematic investigation of the postbuckling behavior and reconfigurability of a representative class of cross-shaped 2D precursor structures, through combined analytical modeling, numerical simulations, and experimental measurements. By formulating an analytic solution to the deformed configuration of a non-uniform beam structures with an arbitrary number of segments, this paper developed a theoretical model to analyze the stability of two typical buckling modes that emerge during the mechanically-guided assembly. The theoretical model allows the construction of general design diagrams for the reconfigurability of cross-shaped precursor structures with different numbers of creases. Furthermore, we demonstrate the extension of the developed model to the bistability analyses of precursor structures with generalized cross patterns or cross-shaped patterns consisting of locally stiffened elements.

2. A theoretical model of postbuckling and bistability of cross-shaped structures

Consider a centrosymmetric cross-shaped structure that consists of four identical ribbon substructures with uniform thicknesses, as schematically shown in Fig. 2a. Considering the symmetry of the geometry and loading conditions, we just need to investigate the deformations of a single substructure. Each ribbon substructure contains a certain number ($n = n_1 + n_2$) of uniform-width segments, including a number (n_1) of creases with reduced width as compared to the other segments (n_2 in total). Since the thickness of the ribbon structure is typically much smaller than the length of each segment, the Euler beam theory is adopted to model their deformations.

In this section, we first derive the governing equations of each uniform-width beam segment in Section 2.1, and then introduced a perturbation method to yield a general analytic solution of rotational angle in Section 2.2. By incorporating the continuity conditions and boundary conditions of the ribbon substructure in Section 2.3, we determine the deformed configurations of two buckling modes and a critical intermediate state, from which the corresponding strain energies are calculated for the stability analyses. Section 2.4 illustrates the validation of the developed model by experiments and FEA.

2.1. Basic equations

Consider a uniform-width beam that deforms in the X-Y plane (Fig. 2b). Due to the slender geometry of the ribbon structure, the axial deformations are usually negligible such that the arc length of the beam does not change after deformation. Then the equilibrium equation of a micro-element (dS) in the beam can be given by

$$\frac{dM}{dS} + f_x \sin\theta - f_y \cos\theta = 0, \quad (1)$$

where f_x and f_y are the reaction force components along the x and y directions at the left end of the beam, respectively; and θ and M are the rotation angle and the bending moment, respectively.

For a linear elastic material with the Young's modulus E , the bending moment M in the beam is given by

$$M = EI \frac{d\theta}{dS}, \quad (2)$$

where EI is the bending stiffness of the beam.

According to Eqs. (1) and (2), the governing equation of a uniform-width beam can be obtained, i.e.,

$$\begin{cases} \frac{d^2\theta}{dS^2} + \frac{1}{EI} (f_x \sin\theta - f_y \cos\theta) = 0, S \in (0, L) \\ \theta|_{S=0} = \theta_l, \frac{d\theta}{dS}|_{S=0} = \frac{M_l}{EI} \end{cases}, \quad (3)$$

where θ_l and M_l are the rotation angle and bending moment at the left end of the beam, and L is the arc length of the beam.

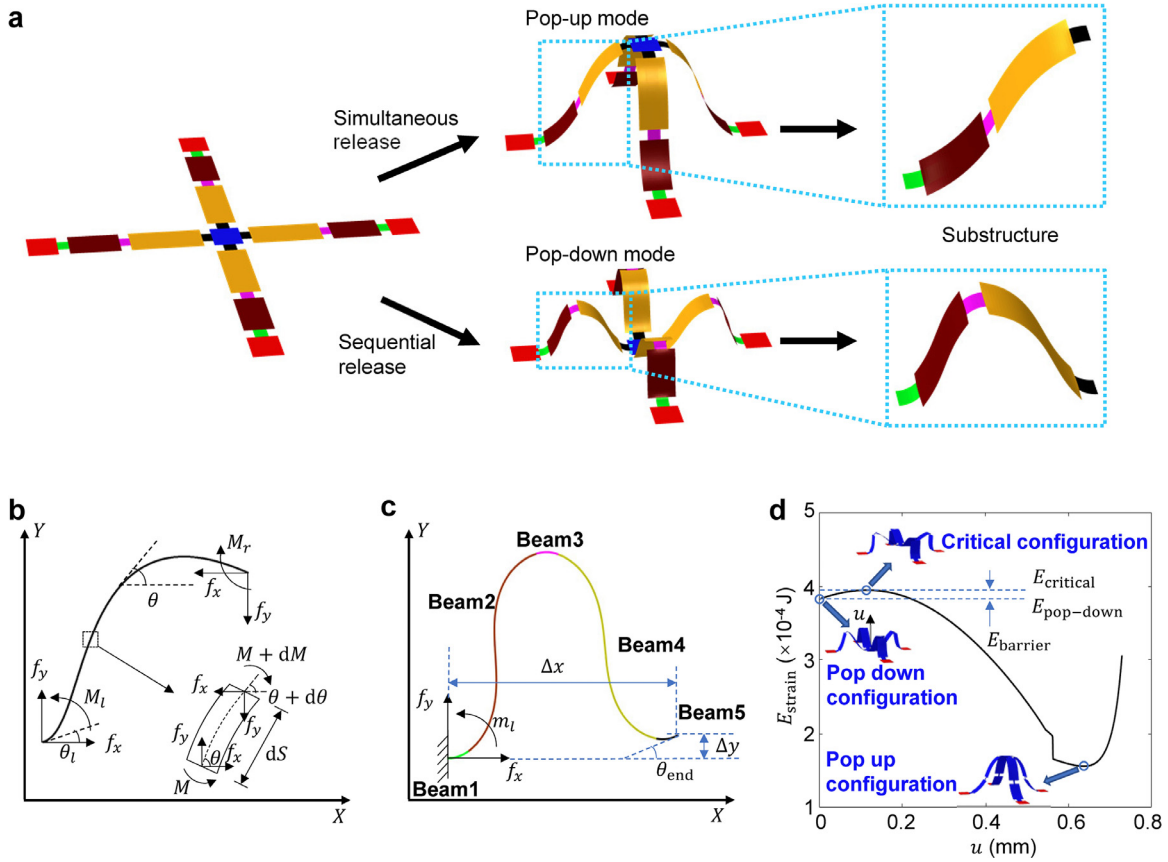


Fig. 2. Illustration of the theoretical model for the bistability analysis of a cross-shaped structure through the loading-path controlled mechanical assembly. (a) Schematic illustration of a cross-shaped 2D precursor, the assembled 3D structures with two different modes, and the ribbon substructures. (b) Free-body diagram of a deformed beam with a uniform cross section, and a unit length element in the beam. (c) Schematic of a ribbon substructure with five segments, in which each segment marked by different color has a uniform cross section. (d) Strain energy as a function of the out-of-plane displacement for a typical cross-shaped structure with three creases in the substructure. The insets show the configurations at three different out-of-plane displacements.

Given the forces (f_x, f_y) and bending moment M_l , Eq. (3) has a unique solution $\theta(S)$, as detailed subsequently in Section 2.2, which describes the deformed configuration of the beam. The bending moment of the right end of the beam can be then calculated by

$$M_r = EI \frac{d\theta}{ds} \Big|_{S=L}. \quad (4)$$

2.2. Perturbation method

The perturbation method is used to solve the governing equation (Eq. (3)) of a uniform-width beam. Specifically, we choose a small parameter μ that is proportional to M_l , such that the angle θ and arc length S can be normalized as:

$$\begin{cases} \bar{\theta} = \frac{1}{\mu}(\theta - \theta_p), \\ \bar{S} = pS \end{cases}, \quad (5)$$

where the parameters θ_p , p and μ are defined as:

$$\begin{cases} \theta_p = \arctan\left(\frac{f_y}{f_x}\right), \quad \theta_p \in \left(-\frac{\pi}{2}, \frac{\pi}{2}\right) \\ p = \sqrt{\frac{\sqrt{f_x^2 + f_y^2}}{EI}} \\ \mu = \frac{M_l}{EIp} \end{cases}. \quad (6)$$

Substitution of Eqs. (5) and (6) into Eq. (3) gives

$$\begin{cases} \frac{d^2\bar{\theta}}{d\bar{S}^2} + \frac{1}{\mu} \sin(\mu\bar{\theta}) = 0 \\ \bar{\theta}|_{\bar{S}=0} = \frac{\theta_l - \theta_p}{\mu}, \quad \frac{d\bar{\theta}}{d\bar{S}}|_{\bar{S}=0} = 1 \end{cases}. \quad (7)$$

According to the perturbation method, the rotation angle $\bar{\theta}(\bar{S})$ can be expanded as:

$$\bar{\theta}(\bar{S}) = \theta_0(\bar{S}) + \theta_1(\bar{S})\mu + \theta_2(\bar{S})\mu^2 + \theta_3(\bar{S})\mu^3 + \theta_4(\bar{S})\mu^4 + \theta_5(\bar{S})\mu^5 + \theta_6(\bar{S})\mu^6 + \dots \quad (8)$$

Substitution of Eq. (8) into Eq. (7) gives a series of perturbation equations:

$$\left\{ \begin{array}{l} \ddot{\theta}_0 + \theta_0 = 0 \\ \ddot{\theta}_1 + \theta_1 = 0 \\ \ddot{\theta}_2 + \theta_2 - \frac{1}{6}\theta_0^3 = 0 \\ \ddot{\theta}_3 + \theta_3 - \frac{1}{2}\theta_1\theta_0^2 = 0 \\ \ddot{\theta}_4 + \theta_4 - \frac{1}{2}\theta_2\theta_0^2 - \frac{1}{2}\theta_0\theta_1^2 + \frac{1}{120}\theta_0^5 = 0 \\ \ddot{\theta}_5 + \theta_5 + \frac{1}{24}\theta_0^4\theta_1 - \frac{1}{2}\theta_3\theta_0^2 - \theta_2\theta_0\theta_1 - \frac{1}{6}\theta_1^3 = 0 \\ \ddot{\theta}_6 + \theta_6 - \frac{1}{2}\theta_0\theta_2^2 - \frac{1}{2}\theta_4\theta_0^2 + \frac{1}{24}\theta_0^4\theta_2 - \frac{1}{5040}\theta_0^7 = 0 \\ \dots \end{array} \right. \quad (9)$$

The boundary conditions of the perturbation equations are given by

$$\left\{ \begin{array}{l} \theta_0(0) = \frac{\theta_l - \theta_p}{\mu}, \dot{\theta}_0(0) = 1 \\ \theta_i(0) = 0, \dot{\theta}_i(0) = 0, i = 1, 2, 3, \dots \end{array} \right. \quad (10)$$

By neglecting the minor terms of the exact solution to Eq. (9) (see Supplementary Information for details), an approximate solution can be obtained as

$$\left\{ \begin{array}{l} \theta_0(\bar{S}) = a \operatorname{Re} \left[e^{i(\bar{S}+\varphi)} \right] \\ \theta_1(\bar{S}) = 0 \\ \theta_2(\bar{S}) = a^3 \operatorname{Re} \left[\frac{e^{i(\bar{S}+3\varphi)}}{96} - \frac{e^{i(\bar{S}-\varphi)}}{32} - \frac{e^{i(\bar{S}-3\varphi)}}{192} + \frac{1-2i\bar{S}}{32} e^{i(\bar{S}+\varphi)} - \frac{e^{i(3\bar{S}+3\varphi)}}{192} \right] \\ \theta_3(\bar{S}) = 0 \\ \theta_4(\bar{S}) = a^5 \operatorname{Re} \left[\frac{-23+20i\bar{S}}{6144} e^{i(\bar{S}-\varphi)} + \frac{3+2i\bar{S}}{3072} e^{i(\bar{S}+3\varphi)} + \frac{1+20i\bar{S}}{61440} e^{i(\bar{S}+5\varphi)} + \frac{13-20i\bar{S}-8\bar{S}^2}{4096} e^{i(\bar{S}+\varphi)} \right. \\ \left. - \frac{3-8i\bar{S}}{12288} e^{i(\bar{S}-3\varphi)} + \frac{e^{i(\bar{S}-5\varphi)}}{10240} + \frac{e^{i(3\bar{S}-\varphi)}}{12288} - \frac{3-4i\bar{S}}{4096} e^{i(3\bar{S}+3\varphi)} - \frac{e^{i(3\bar{S}+5\varphi)}}{6144} + \frac{e^{i(3\bar{S}+\varphi)}}{2048} \right] \\ \theta_5(\bar{S}) = 0 \\ \theta_6(\bar{S}) = a^7 \operatorname{Re} \left[\frac{-165+155i\bar{S}+42\bar{S}^2}{294912} e^{i(\bar{S}-\varphi)} + \frac{117-140i\bar{S}}{82575360} e^{i(\bar{S}-7\varphi)} + \frac{49+50i\bar{S}+30\bar{S}^2}{491520} e^{i(\bar{S}+3\varphi)} \right. \\ \left. - \frac{113-28i\bar{S}}{41287680} e^{i(\bar{S}+7\varphi)} + \frac{37+68i\bar{S}+60\bar{S}^2}{1966080} e^{i(\bar{S}-3\varphi)} + \frac{523-872i\bar{S}-288\bar{S}^2+48i\bar{S}^3}{1179648} e^{i(\bar{S}+\varphi)} \right. \\ \left. + \frac{205-152i\bar{S}}{5898240} e^{i(\bar{S}-5\varphi)} - \frac{105-338i\bar{S}-120\bar{S}^2}{5898240} e^{i(\bar{S}+5\varphi)} \right] \end{array} \right. \quad (11)$$

where $a = \sqrt{1 + (\frac{\theta_l - \theta_p}{\mu})^2}$ and $\varphi = 2\pi - \arccos(\frac{\theta_l - \theta_p}{\mu a})$. Note that the coefficients of the odd power terms in the expansion (Eq. (8)) can be proved to be zero (see Supplementary Information for details), which simplifies the calculations.

Till now, the explicit expression of $\theta(S)$ in terms of the reaction force components (f_x , f_y , and M_l) is obtained, which can be denoted as $\theta(S; f_x, f_y, M_l)$. Once the components f_x , f_y , M_l , are determined, the deformed configuration of the beam can be obtained.

2.3. Stability analyses

The continuity conditions require that the rotation angle, moment and force components are continuous at the connection points of different beam segments in the substructure. Taking a ribbon substructure with five uniform-width segments as an example (Fig. 2c), the continuity conditions between the i th and $(i+1)$ th beam segments can be written as

$$\left\{ \begin{array}{l} \theta^{(i)}(L_i) = \theta^{(i+1)}(0) \\ M_r^{(i)} = M_l^{(i+1)} \\ f_x^{(i)} = f_x^{(i+1)} = f_x \\ f_y^{(i)} = f_y^{(i+1)} = f_y \end{array} \right. , \quad i = 1, 2, 3, 4, \quad (12)$$

where $M_l^{(i)}$ and $M_r^{(i)}$ are the bending moments of the left and right ends of the i th beam, respectively; $\theta^{(i)}(S)$ is the rotation angle of the i th beam; and L_i is the length of the i th beam.

With use of Eqs. (4), (8), (11) and (12), the rotation angle $\theta^{(i)}(S)$ in the entire substructure can be obtained for prescribed force components ($f_x, f_y, M_l^{(1)}$) and rotation angle ($\theta^{(1)}(0)$) at the left end of the 1st beam, by iterating the following steps:

- (1) Calculate the bending moment $M_r^{(i)}$ and the rotation angle $\theta^{(i)}(L_i)$ at the right end of the i th beam based on $M_l^{(i)}$ and $\theta^{(i)}(0)$ at the left end, according to Eqs. (4), (8) and (11);

- (2) Calculate the bending moment $M_l^{(i+1)}$ and the rotation angle $\theta^{(i+1)}(0)$ at the left end of the $(i+1)$ th beam according to the continuity conditions (Eq. (12)).

Note that the force components $(f_x, f_y, M_l^{(1)})$ at the left end are usually unknown and need to be determined by the boundary conditions of the ribbon substructure. Considering the process of mechanically-guided 3D assembly, the ribbon substructure can be modeled as clamped at the left end, as shown in Fig. 2c. Due to the geometric symmetry, the rotational angle at the right end of the substructure is also zero during the deformation. For a given prestrain $\epsilon_{\text{prestrain}}$ of substrate in the 3D assembly, the deformed span (Δx) of the substructure can be determined by

$$\Delta x = L_{\text{total}} / (1 + \epsilon_{\text{prestrain}}). \quad (13)$$

where $L_{\text{total}} = \sum_{i=1}^5 L_i$ is the total arc length of the substructure.

In the meanwhile, the relative distances ($\Delta X, \Delta Y$) between the two ends of the substructure and the rotation angle (θ_{end}) at the right end of the beam can be calculated by

$$\begin{cases} \Delta X(f_x, f_y, M_l) = \sum_{i=1}^5 \int_0^{L_i} \cos \theta^{(i)} dS \\ \Delta Y(f_x, f_y, M_l) = \sum_{i=1}^5 \int_0^{L_i} \sin \theta^{(i)} dS \\ \theta_{\text{end}}(f_x, f_y, M_l) = \theta^{(5)}(L_5) \end{cases}. \quad (14)$$

The strain energy of the substructure can be calculated by

$$U_e = \sum_{i=1}^5 \int_0^{L_i} \frac{1}{2} (EI)_i \left(\frac{d\theta_i}{dS} \right)^2 dS. \quad (15)$$

Then we analyze the stability of the two possible buckling modes (Shapes I and II), which are termed as pop-up and pop-down modes in this study. For this, we can study the energy profile of the substructure by applying an increasing out-of-plane displacement ($\Delta y = u$) to the right end, according to our previous work (Fu et al., 2018). As shown in Fig. 2d for a representative design, the pop-down mode typically denotes the configuration with zero out-of-plane displacement ($\Delta y = 0$), and the pop-up mode corresponds to an energy minimal state at a finite out-of-plane displacement. Between these two modes in the energy profile, there is a critical configuration that gives a local energy maximal. The stability of the pop-down mode then depends highly on the magnitude of energy barrier ($E_{\text{barrier}} = E_{\text{critical}} - E_{\text{pop-down}}$) between the critical configuration and the pop-down mode. The following sub-sections describe the boundary conditions and the calculation method for these three important configurations.

2.3.1. Configuration of the pop-down mode

The boundary conditions of the pop-down configuration are given by $\Delta X = \Delta x$, $\Delta Y = 0$, and $\theta_{\text{end}} = 0$. Then the three nonlinear governing equations in terms of three independent variables (f_x, f_y, M_l) can be written as

$$\begin{cases} \Delta X(f_x, f_y, M_l) = \Delta x \\ \Delta Y(f_x, f_y, M_l) = 0 \\ \theta_{\text{end}}(f_x, f_y, M_l) = 0 \end{cases} \quad (16)$$

By using the trust-region-dogleg method, this set of nonlinear equations Eq. (16), together with Eqs. (5), (6), (8), (11)–(14), can be solved numerically (Coleman and Li, 1996), from which the force components (f_x, f_y, M_l) are determined. This method assumes that the nonlinear function is quadratic within the “trust region”, and then solves the constrained optimization problem of quadratic functions in the “trust region”. If the optimized value is obtained at the boundary of the trust region, it uses the dogleg method to move and shrink the trust region of the next iteration step to approach the global optimal point gradually. This method is effective in solving nonlinear equations with a strong nonlinearity. The deformed configuration of the pop-down mode and the corresponding strain energy ($E_{\text{pop-down}}$) can be then obtained from Eqs. (5), (6), (8), (11)–(15).

2.3.2. Critical configuration

As illustrated in Fig. 2d, the critical configuration corresponds to the state when the strain energy (U_e) reaches a local maximum, i.e., $\frac{\partial U_e}{\partial u} = 0$. According to the energy principle, the y -directional force component (f_y) is also equal to the derivative of the strain energy with respect to the displacement (u), i.e., $f_y = \frac{\partial U_e}{\partial u}$. This indicates that f_y is zero at the critical configuration. Then the boundary conditions to determine the critical configuration can be written as

$$\begin{cases} \Delta X(f_x, M_l) = \Delta x \\ \theta_{\text{end}}(f_x, M_l) = 0 \\ \frac{\partial^2 U_e(f_x, M_l)}{\partial u^2} < 0 \end{cases} \quad (17)$$

Here we just have two independent variables (f_x and M_l). This set of nonlinear equations (Eq. (17)) are also solved numerically using the trust-region-dogleg method (Coleman and Li, 1996). Then the force components and the strain energy (E_{critical}) of the critical configuration can be obtained.

2.3.3. Configuration of the pop-up mode

The strain energy reaches the local energy minimum at the pop-up mode, and therefore $\frac{\partial U_e}{\partial u} = 0$ and $\frac{\partial^2 U_e}{\partial u^2} > 0$. This also requires that $f_y = 0$. Then the boundary conditions to determine the force components (f_x and M_l) of the pop-up mode can be written as

$$\begin{cases} \Delta X(f_x, M_l) = \Delta x \\ \theta_{\text{end}}(f_x, M_l) = 0 \\ \frac{\partial^2 U_e(f_x, M_l)}{\partial u^2} > 0 \end{cases} \quad (18)$$

Similarly, we exploit the trust-region-dogleg method to solve the nonlinear equations (Eq. (18)) numerically (Coleman and Li, 1996). The deformed configuration of the pop-up mode and the corresponding strain energy ($E_{\text{pop-up}}$) can be then determined.

2.3.4. Stability coefficient

As reported by our previous work (Fu et al., 2018), the magnitude of energy barrier ($E_{\text{barrier}} = E_{\text{critical}} - E_{\text{pop-down}}$) is crucial to the stability of the pop-down mode, and the structures with relative large energy barriers tend to maintain the pop-down mode after the prestrain release. Here, we propose a dimensionless energy barrier normalized by the strain energy ($E_{\text{pop-down}}$) to quantify the stability of pop-down mode, which is given by

$$E_r = \frac{E_{\text{barrier}}}{E_{\text{pop-down}}}. \quad (19)$$

This stability coefficient E_r can be calculated once the strain energies ($E_{\text{pop-down}}$ and E_{critical}) are determined, as described in Sections 2.3.1 and 2.3.2.

2.4. Validation of the theoretical model

Both the experiments and FEA were carried out to validate the theoretical model described above. In the experiments, the planar cross-shaped precursor structures were patterned from polyimide film (PI; 75 μm in thickness), using automatic mechanical cutting. A silicone film (3 mm in thickness, Dragon Skin, Smooth-On, USA) served as the assembly substrate. A commercial adhesive (Super Glue, Gorilla Glue Company, Cincinnati, USA) dispensed at the bonding areas of the cross-shaped precursor fixed the structure with the substrate. Releasing the prestrain slowly (strain rate < 20%/min) in the substrate with different sequences completed the assembly of 3D bistable structures. In the FEA, we used the commercial software ABAQUS to model the deformations of cross-shaped structures, under both the loading conditions of simultaneous compression and sequential compression. The shell elements (S4R) were adopted for the ribbon structure, and refined meshes ensured the computational accuracy. The buckling mode determined from a linear perturbation analyses was implemented as a type of geometric imperfections in the simulations of postbuckling process. A linear-elastic relation was adopted for PI (Young's modulus 2.5 GPa and Poisson's ratio 0.34).

Fig. 3 shows the evolution of deformed configurations during the sequential and simultaneous releases of prestrain for two representative cross-shaped patterns, one with three creases (Fig. 3a) and the other with a single crease (Fig. 3b) in a substructure of the design. In both cases, the deformed configurations predicted by the theoretical model agree well with the results of FEA calculations and experimental measurement. It is noteworthy that the thickness of cross-shaped structures should be carefully selected, since a thick design could possibly result in the delamination of the bonding sites and the failure of the material. Quantitative mechanics calculations (see Supplementary Information for details) can serve as a guideline for the thickness design to avoid these issues.

3. Bistability analyses of cross-shaped structures

The developed model in Section 2 allows us to construct general design diagrams with respect to the bistability of the cross-shaped precursor structures. The three key geometric parameters investigated in this section include the number, the width and the position of creases in the substructure. The following three sub-sections analyze the bistability of cross-shaped designs with one, two and three creases in a substructure, respectively.

3.1. Cross-shaped structures with a single crease in the substructure

Depending on their positions, the creases are classified into three categories, including the α crease located at the right end of the substructure (i.e., the center of the cross pattern), the β crease located in the inner region of the substructure, and the γ crease at the left end of the substructure (i.e., the connection with the bonding sites). This section focuses on the design with a single crease (either α , β or γ crease) in the substructure.

Consider a cross-shaped pattern with a single α crease, as shown in Fig. 4a. Here, we just vary the width of the crease to study the effect of crease stiffness on the bistability, noting that the length of the crease plays a similar role (Fu et al., 2018). Then the unique design parameter is the factor of width reduction at the crease, as denoted by $\omega_\alpha = W_\alpha/W$, where W_α and W are widths of the crease and the other regions. The length of the crease is fixed as 0.1l, where l is the total

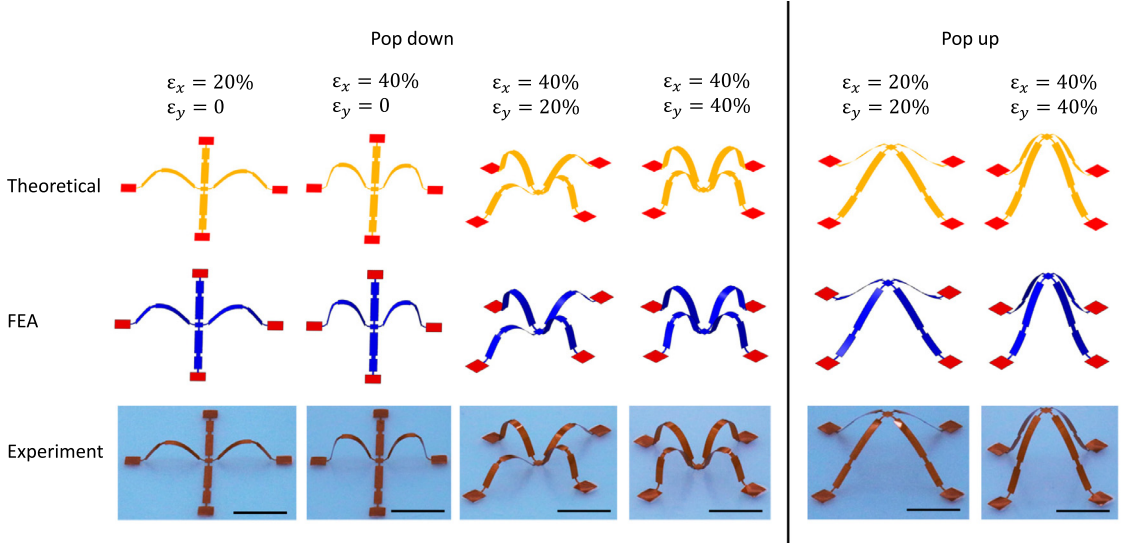
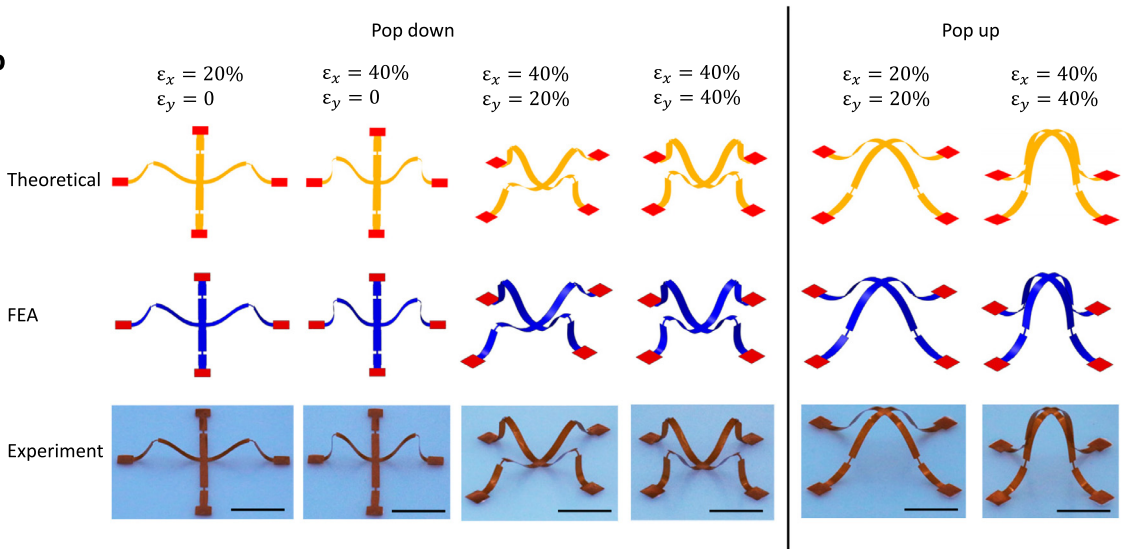
a**b**

Fig. 3. Validation of the theoretical model. (a) Experimental, theoretical and FEA results for the deformed configurations during the assembly of a cross-shaped structure with the design parameters of $(\omega_\alpha, \omega_\beta, \omega_\gamma, \eta_\beta) = (0.2, 0.5, 0.2, 0.65)$ by sequential loading (left panel) and simultaneous loading (right panel). (b) Similar results for a cross-shaped structure with the design parameters of $(\omega_\alpha, \omega_\beta, \omega_\gamma, \eta_\beta) = (0.9, 0.2, 0.9, 0.65)$. The definition of these parameters can be found in Fig. 7a. Scale bars, 2 cm.

arc length of the substructure excluding the crease regions. Fig. 4b presents the results of stability coefficient E_r at different dimensionless crease widths, based on the calculations of exact analytic model (without neglecting the minor terms in the solution to Eq. (9)), approximate analytic model (using the approximate solution Eq. (11)) and FEA. Both the predictions of exact model and approximate model agree well with the FEA results. All of the results show that the stability coefficient E_r increases with decreasing the dimensionless crease width ω_α , indicating that ω_α should be sufficiently small to achieve reconfigurable 3D structures through the loading-path strategy.

During the process of 3D assembly in experiments, slight imperfections, such as parasitic adhesion/stiction at regions adjacent to the bonding sites, can introduce external disturbance that may be significant as compared to the energy barrier. As a result, the same 2D precursor might not always form the pop-down mode during the sequential release, for a large number (e.g., > 20) of samples. To investigate the relationship between the stability coefficient E_r and the possibility to form the pop-down configuration during sequential release, statistical studies were performed for cross-shaped patterns with five different crease widths ($\omega_\alpha = 0.3, 0.5, 0.6, 0.67$ and 0.7), marked as P1 to P5 in Fig. 4b, respectively. Taking the design point P3 as an example, four 3×3 arrays of the cross-shaped patterns were fabricated and each array was chemically bonded to

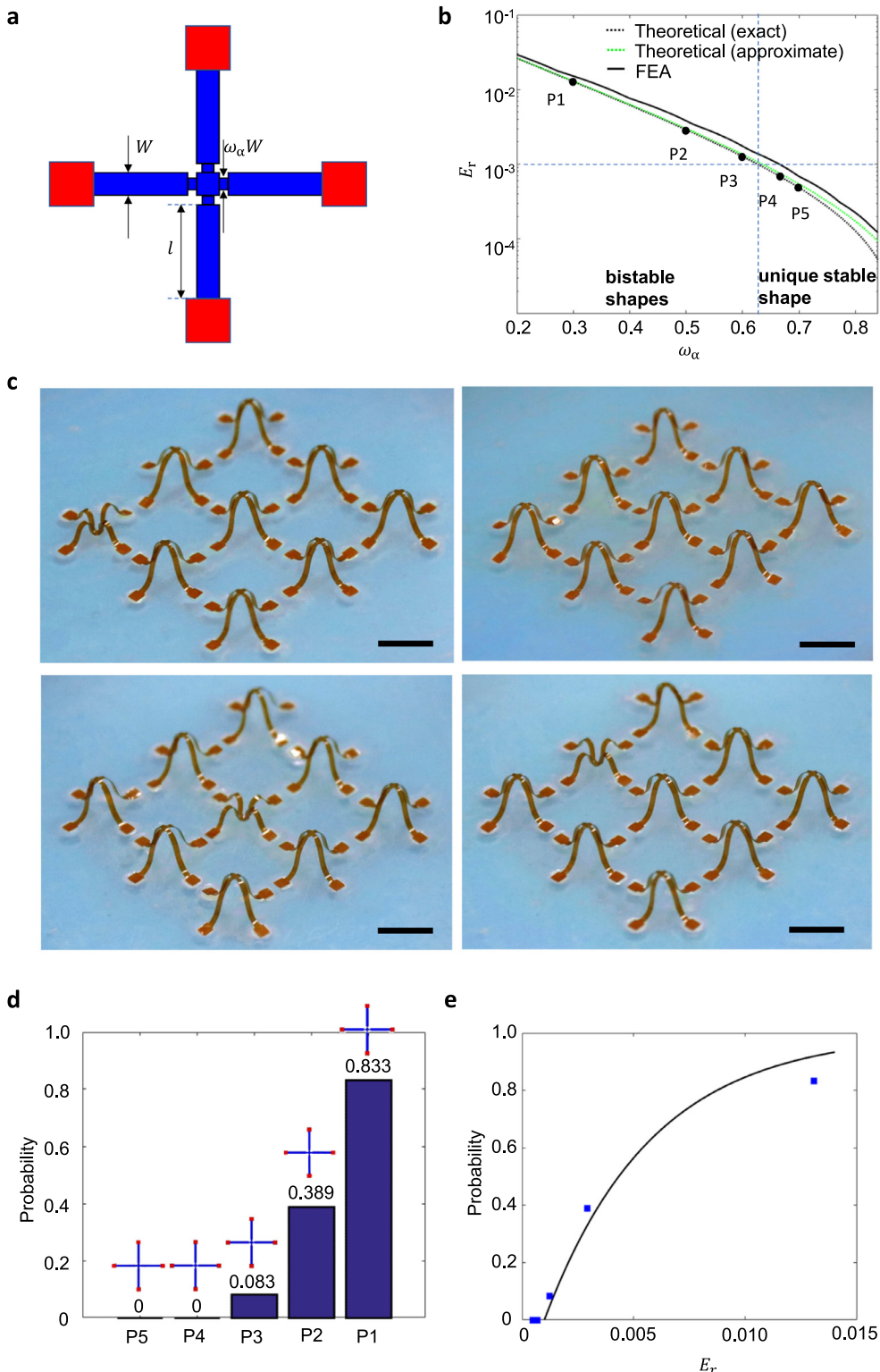


Fig. 4. Bistability analysis for the cross-shaped structure with a single α crease. (a) Illustration of the geometric parameters for this cross-shaped structure, where the length of the crease is fixed as $0.1l$. (b) Stability coefficient E_r as a function of the width ratio ω_α . (c) Probabilistic experimental results for the design point P3 in (b). Scale bars, 1 cm. (d) Experimentally determined probability for achieving the pop-down shape by sequential release. (e) Dependence of the probability on the stability coefficient E_r .

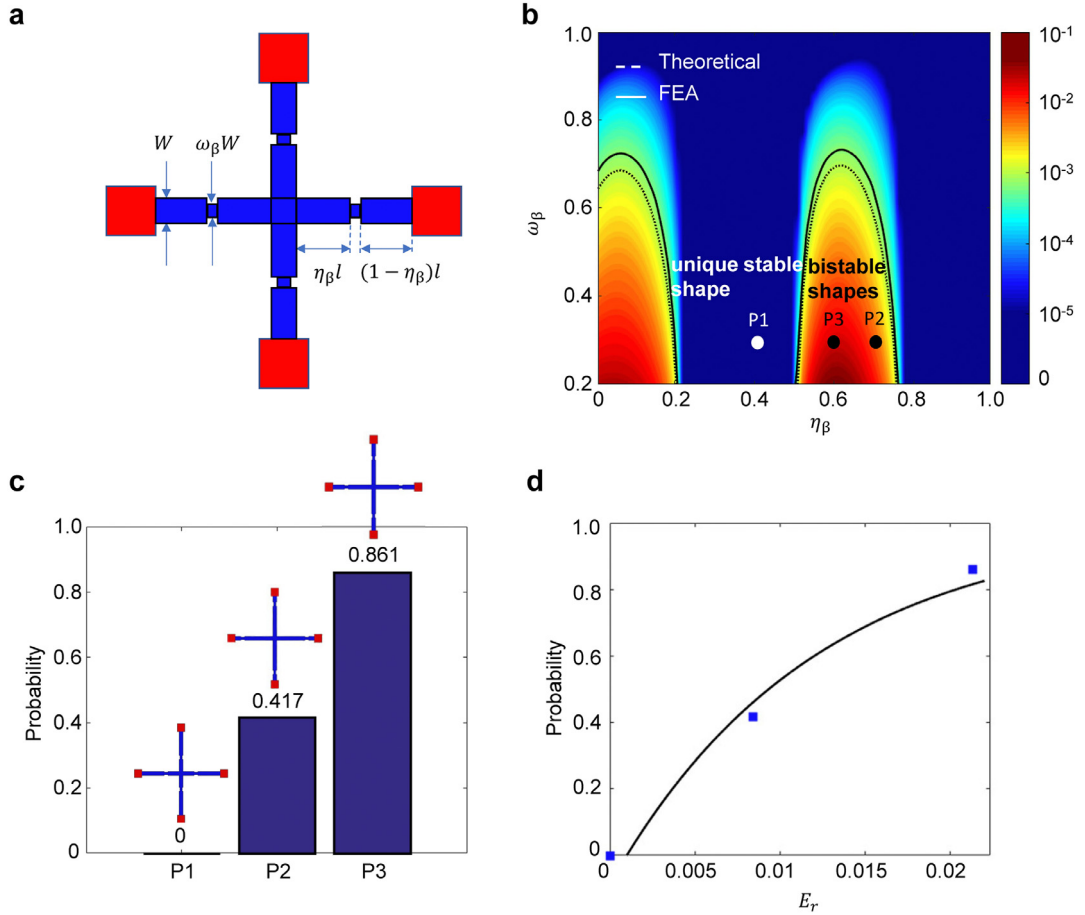


Fig. 5. Bistability analysis for the cross-shaped structure with a single β crease. (a) Illustration of the geometric parameters for this cross-shaped structure, where the length of the crease is fixed as $0.1l$. (b) Contour plot of the stability coefficient E_r in terms of the design parameters η_β and ω_β . (c) Experimentally determined probability for achieving the pop-down shape by sequential release. (d) Dependence of the probability on the stability coefficient E_r .

a prestrained silicone substrate (Fig. 4c). Then the prestrain was sequentially released in all of the four substrates to form buckled architectures, and the number of pop-down configuration was counted over all of the 36 samples to calculate the probability, as shown in Fig. 4d and Figure S1 (Supplementary Information). This type of experiment was repeated three times to record the probability, and a good repeatability can be observed. According to the statistical results in Fig. 4e, the probability (P) to form pop-down configurations increases rapidly with increasing the stability coefficient (E_r). For the structures with stability coefficient $E_r < 0.001$, the probability to form pop-down configuration becomes zero, indicating that the pop-down mode cannot be achieved during the sequential loading. As such, a simple criterion to judge the reconfigurability of the cross-shaped patterns can be introduced as $E_r \geq E_{threshold}$, where $E_{threshold}$ is the threshold of stability coefficient to enable bistable configurations. This threshold is taken as 0.001, according to the theoretical and experimental results. Based on this criterion, two design domains can be identified in Fig. 4b, namely “bistable shapes” and “unique stable shape”. The design parameters in the right domain (with $E_r < 10^{-3}$) can only yield a unique stable shape (i.e., the pop-up mode), under both sequential and simultaneous loadings. On the contrary, the design parameters in the left domain (with $E_r > 10^{-3}$) can possibly yield bistable buckling modes with a certain probability. Inspired by the Boltzmann distribution, an exponential law can be introduced to describe the dependence of probability (P) on the stability coefficient (Fu et al., 2018), as expressed by

$$P = 1 - e^{-k(E_r - E_{threshold})}, \quad E_r > E_{threshold} \quad (20)$$

where $k = 208.2$ is a dimensionless fitting parameter. Similar exponential distributions were also observed in a few multi-stable dynamic systems (Ashwin et al., 2017; Christ et al., 2017).

Fig. 5a shows another representative case of the cross-shaped pattern, with a single β crease in the substructure. Here, the location of crease denoted by the dimensionless parameter (η_β) represents another design parameter, in addition to the dimensionless width (ω_β) of crease. Fig. 5b and Figure S2 (Supplementary Information) present the theoretical predictions and FEA results of the stability coefficient E_r in a wide range of η_β and ω_β . The curved dashed line (theoretical) and

solid line (FEA) that correspond to $E_r = 10^{-3}$ are marked in the contour plot. The regime outside these black curves yields the same configuration (i.e., pop-up mode) for simultaneous and sequential release, due to the insufficiently large energy barrier. Within these curves, the pop-down mode can stabilize, thereby offering the capability of achieving reconfigurable 3D structures. This suggests that the crease should be placed near the positions of $\eta_\beta=0.05$ or $\eta_\beta=0.6$, and should be narrow enough ($\omega_\beta < 0.65$). As the parameter η_β approaches 1, the β crease degenerates into a γ crease. Because of the vanishing stability coefficient, the design with a single γ crease can only yield a unique stable shape through the loading-path strategy. On the other hand, as the parameter η_β approaches 0, the β crease degenerates into an α crease, and the profile of contour plot at $\eta_\beta = 0$ coincides with that in Fig. 4b. This set of results also provides further evidence about the accuracy of the theoretical model.

Statistic experiments were carried out for three representative design points marked by 'P1', 'P2' and 'P3' in Fig. 5b. For each design point, the probability was determined from the experiments over 36 samples, similar to that in Fig. 4. The results appear in Fig. 5c,d and Figure S3 (Supplementary Information). The design point 'P1' that falls in the "unique stable shape" domain can only form the pop-up configuration. For the two design points ('P2' and 'P3') in the "bistable shapes" domain, the one with a larger stability coefficient E_r has a higher probability to achieve stable pop-down configurations. In this case, the probability (P) to form pop-down configurations during sequential release also follows an exponential dependence (Eq. (20)) on the stability coefficient E_r , as shown in Fig. 5d, with the fitting parameter $k = 83.25$.

3.2. Cross-shaped structures with two creases in the substructure

We first focus on the cross-shaped pattern with the coexistence of α and β creases. As shown in Fig. 6a, the geometry is characterized by three parameters, including two dimensionless crease widths (ω_α and ω_β) and the normalized position (η_β) of the β crease. Again, the lengths of both creases are fixed as $0.1l$, where l is the total arc length of the substructure excluding the crease regions. Fig. 6b provides the contour plot of stability coefficient E_r in terms of parameters η_β and ω_β , for a representative width ratio $\omega_\alpha = 0.5$. The curve of $E_r = 10^{-3}$ divides the design diagram into the domains of "bistable shapes" and "unique stable shape". Different from the design with a single β crease as discussed in Section 3.1, the boundary of the two domains in the design diagram herein changes dramatically with varying the width ratio ω_α (Fig. 6c and d).

For relatively large width ratios of α crease (e.g., $\omega_\alpha \geq 0.7$), the domain of "bistable shapes" enlarges mainly vertically with decreasing ω_α , as depicted in Fig. 6c. Note that the boundary line becomes identical to the case with a single β crease in Fig. 5b, as ω_α reaches 1. With the further reduction of ω_α (e.g., $\omega_\alpha \leq 0.6$), the boundary of the bistable domain evolves into two branches, as shown in Fig. 6d. As a result, the domain of "unique stable shape" is separated into two isolated regions, and these regions shrink with the reduction of ω_α . As ω_α falls below 0.2, the bistable domain occupies almost the entire design space of $0 < \eta_\beta < 1$ and $0.2 < \omega_\beta < 1$, suggesting that the pop-down mode is quite energy favorable when $\omega_\alpha \leq 0.2$. As shown in Fig. 6d (for $\omega_\alpha \leq 0.6$), when the β crease is positioned in the range of $0.45 < \eta_\beta < 0.75$, the design can yield bistable 3D structures for any value of ω_β , although the probability increases with the decrease of ω_β . In contrast, the design is more probable to form bistable 3D structures at a larger ω_β , when the β crease is positioned in the range of $0.15 < \eta_\beta < 0.4$ or $\eta_\beta > 0.8$, according to the varying trend of the stability coefficient E_r . Note that the β crease degenerates into a γ crease at $\eta_\beta = 1$, and in this condition, the pop-down mode can stabilize only when ω_α is sufficiently small and ω_β is sufficiently large. This indicates that the introduction of γ crease weakens the stability of the pop-down mode.

The design diagram is also validated by statistic experiments performed for three representative examples marked by 'P1', 'P2' and 'P3' in Fig. 6b. Their design parameters are $(\omega_\alpha, \omega_\beta, \eta_\beta) = (0.5, 0.3, 0.3)$ $(0.5, 0.3, 0.7)$ and $(0.5, 0.3, 0.55)$, respectively. Their possibilities to form pop-down configurations are presented in Fig. 6e,f and Figure S4 (Supplementary Information), which also show an exponential dependence on the stability coefficient, similar to the case discussed in Section 3.1. Here, the probability also decreases with decreasing the stability coefficient E_r , and become zero when E_r is below 0.001 for the design point 'P1'.

In the scenario that the cross-shaped pattern contains the β and γ creases, the stability coefficient can be analyzed similarly, with the results shown in Figure S5 (Supplementary Information). With the coexistence of β and γ creases, the domain of "bistable shapes" is obviously smaller than the case with a single β crease.

3.3. Cross-shaped structures with three creases in the substructure

Fig. 7a shows a cross-shaped pattern with the coexistence of α , β and γ creases. This geometry is characterized by four design parameters, including three dimensionless crease widths (ω_α , ω_β and ω_γ) and the normalized position (η_β) of the β crease. This section focuses on a typical condition, in which the widths of α and γ creases are equal to each other, i.e., $\omega_\alpha = \omega_\gamma$. Fig. 7b presents the contour plot of stability coefficient E_r in terms of parameters η_β and ω_β , for a representative width ratio $\omega_\alpha = 0.5$. The boundary curve ($E_r = 10^{-3}$) that divides the design diagram into two domains is marked in the contour plot. The boundary curves are not very sensitive to the change of ω_α , according to both the results of theoretical model and FEA in Fig. 7c. This is distinct from the case with two creases (α and β), as discussed in Section 3.2. Additionally, the domain of "bistable shapes" in Fig. 7c is smaller than that in Fig. 6 (with α and β creases) and larger than that in Figure S5 (Supplementary Information) (with β and γ creases), given the same magnitude of width ratio ω_α or ω_γ . From this set of comparison and the results presented in Sections 3.1 and 3.2, it can be concluded that the stability of pop-down configuration can be enhanced by introducing the α crease, and weakened by introducing the γ crease.

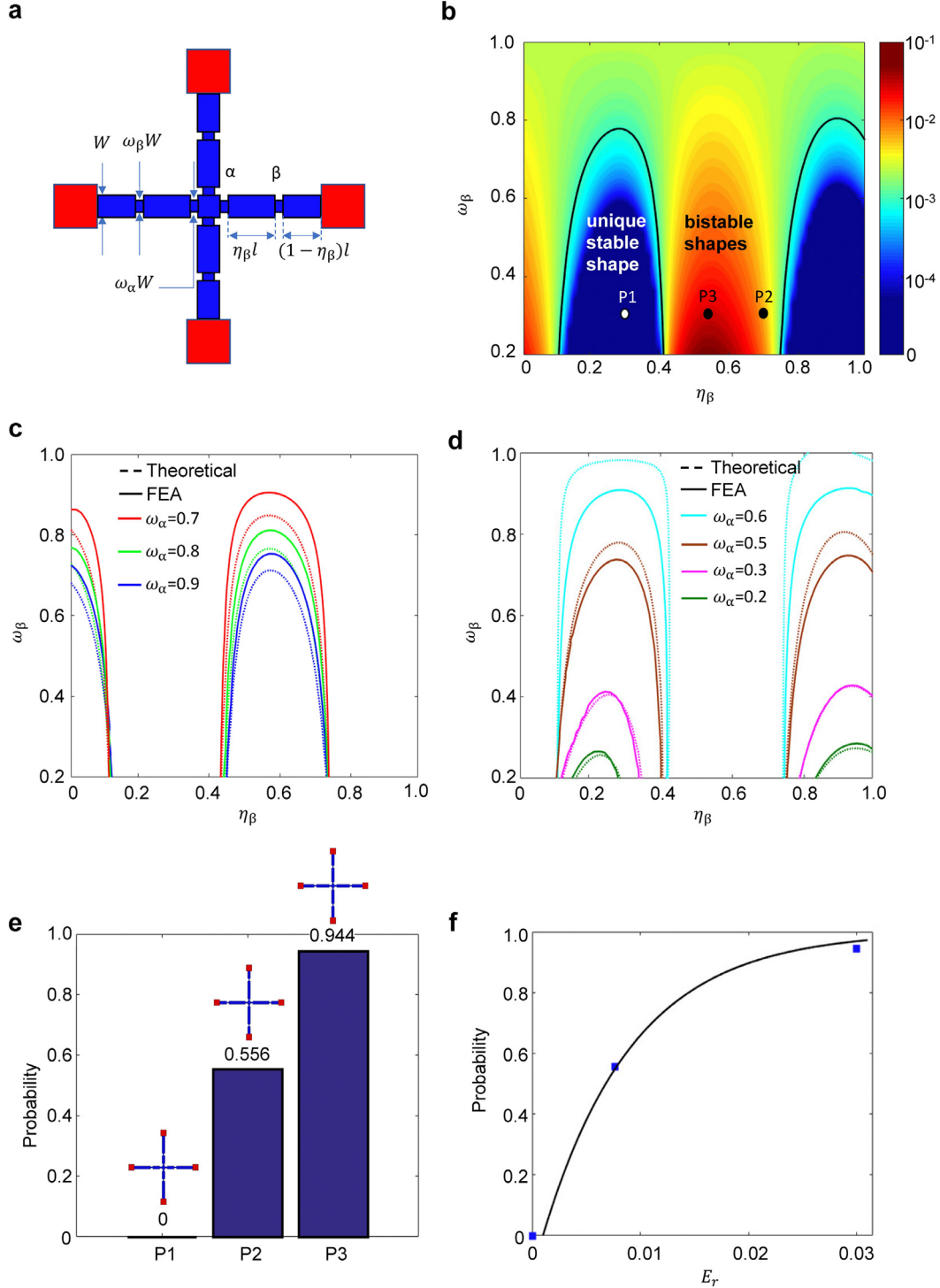


Fig. 6. Bistability analysis for the cross-shaped structure with coexistence of α and β creases. (a) Illustration of the geometric parameters for this cross-shaped structure, where the lengths of both creases are fixed as $0.1l$. (b) Contour plot of the stability coefficient E_r in terms of the design parameters η_β and ω_β , where ω_α is fixed at 0.5. (c, d) Theoretical and FEA results on the design diagrams in the space of design parameter η_β and ω_β , when ω_α varies from 0.7 to 0.9 (c) and from 0.2 to 0.6 (d). (e) Experimentally determined probability for achieving the pop-down shape by sequential release. (f) Dependence of the probability on the stability coefficient E_r .

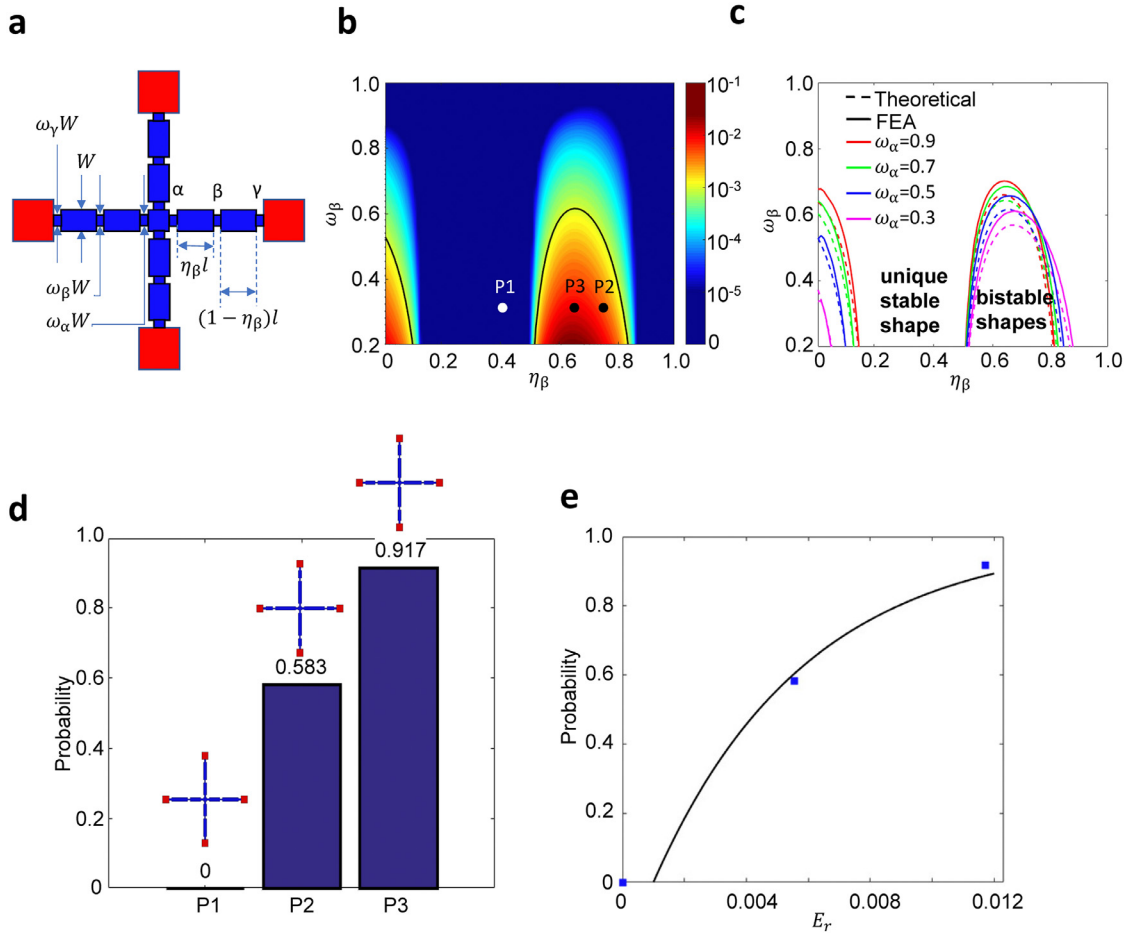


Fig. 7. Bistability analysis for the cross-shaped structure with coexistence of α , β and γ creases. (a) Illustration of the geometric parameters for this cross-shaped structure, where the lengths of all three creases are fixed as $0.1l$. (b) Contour plot of the stability coefficient E_r in terms of the design parameters η_β and ω_β , where ω_α and ω_γ are fixed at 0.5. (c) Theoretical and FEA results on the design diagrams in the space of design parameter η_β and ω_β , when ω_α varies from 0.3 to 0.9. (d) Experimentally determined probability for achieving the pop-down shape by sequential release. (e) Dependence of the probability on the stability coefficient E_r .

Statistic experiments were performed to verify the design diagram in Fig. 7b. Three design points were selected, with their parameters given by $(\omega_\alpha, \omega_\beta, \eta_\beta) = (0.5, 0.3, 0.4)$, $(0.5, 0.3, 0.75)$ and $(0.5, 0.3, 0.65)$, respectively (see Figure S6, Supplementary Information for details). Similar to the cases with one or two creases, the probability to form pop-down configurations also shows a monotonous dependence on the stability coefficient E_r (Fig. 7d and e), and become zero when E_r is below 0.001.

In all of the different cases in Figs. 4–7, the predictions of developed theoretical model agree well with FEA results, suggesting it as a reliable design reference to achieve reconfigurable 3D structures.

4. Extension to other reconfigurable structures

The above theoretical model can be extended to the bistability analyses of other ribbon-shaped 2D precursor structures where no twisting deformations occur. This section provides two demonstrative examples, including generalized crossed patterns with unequal arms and cross-shaped patterns consisting of locally stiffened elements.

4.1. Generalized crossed patterns with unequal arms

Fig. 8a shows a schematic illustration of a generalized crossed pattern consisting of a single α crease in a substructure. Here, the horizontal ribbons are longer than the vertical ribbons, and the creases geometries can vary independently in these ribbons. The geometry of this structure can be characterized by five design parameters, including the length ratio (l_h/l_v), two dimensionless crease widths (ω_h and ω_v), and two position parameters (η_h and η_v), where the subscripts 'h' and 'v' denote the horizontal and vertical ribbons. In the stability analyses, both the strain energies of the horizontal and vertical ribbons

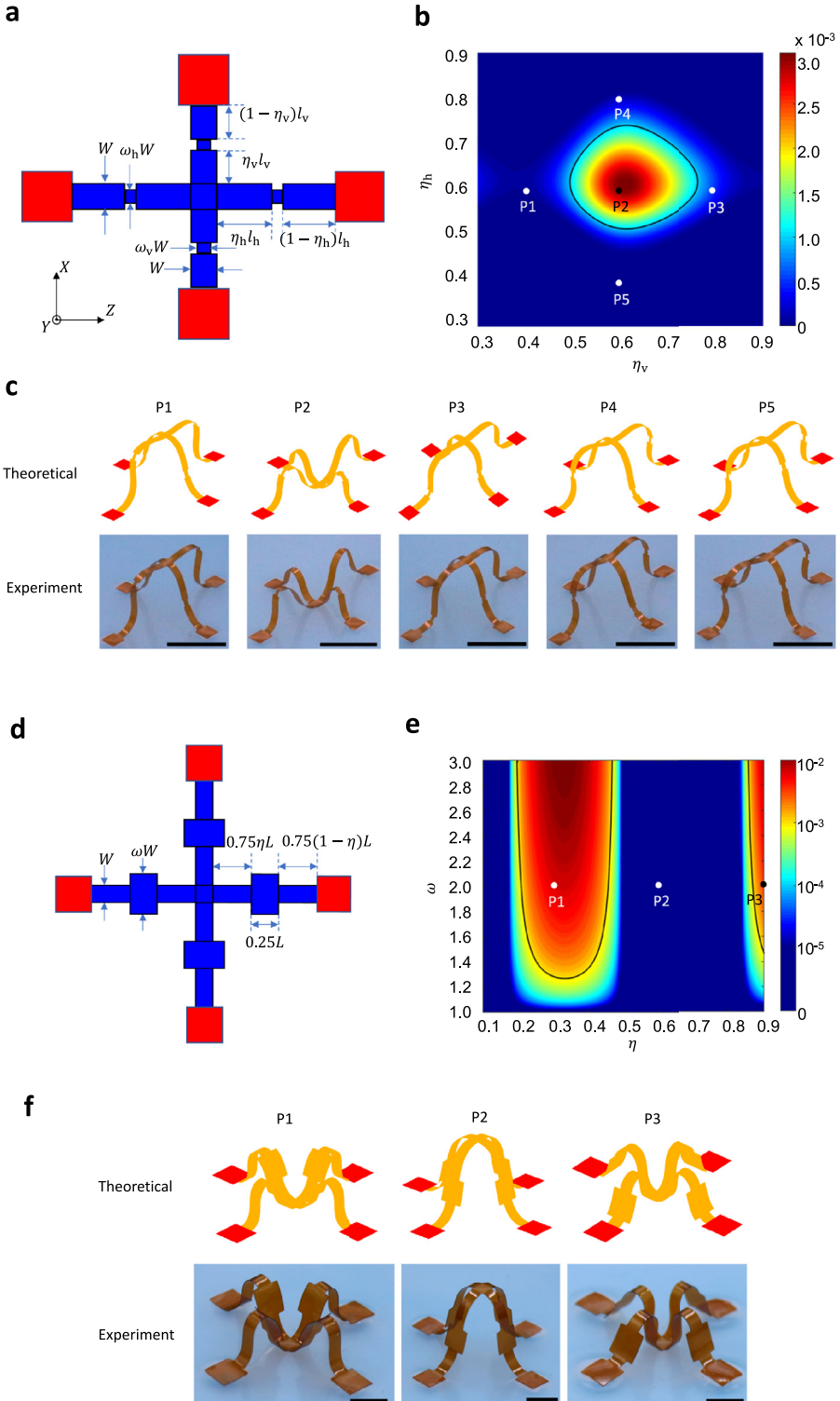


Fig. 8. Bistability analysis for other reconfigurable structures. (a) Illustration of the geometric parameters in a cross-shaped structure with unequal arms, in which the length of crease is $0.1l_a$. (b) Contour plot of the stability coefficient E_r in terms of the design parameters η_h and η_v , where the length ratio is $l_h/l_v = 1.5$, and the width ratios are $\omega_h = 0.4$ and $\omega_v = 0.6$. (c) Experimental and theoretical results on the deformed configurations of the cross-shaped structures (with different design parameters, as marked in (b)) during the sequential loading with 82% equal biaxial prestrain. Scale bars, 2 cm. (d) Illustration of the geometric parameters in a cross-shaped structure with locally stiffened elements. (e) Contour plot of the stability coefficient E_r in terms of the design parameters η and ω . (f) Experimental and theoretical results on the deformed configurations of the cross-shaped structure with locally stiffened elements (with different design parameters, as marked in (e)) during the sequential loading with 82% equal biaxial prestrain. Scale bars, 1 cm.

should be taken into account. Let U_h and U_v denote the strain energies of the horizontal arm and vertical arm, respectively. Then the total strain energy is given by $U_{\text{total}} = U_h + U_v$. At the critical configuration (or the pop-up configuration) discussed in Sections 2.3.2 (or 2.3.3), the total strain energy reaches its maximum (or minimum), such that $\frac{\partial U_{\text{total}}}{\partial u} = 0$. This requires that $f_{yh} + f_{vv} = 0$, where $f_{yh} = \frac{\partial U_h}{\partial u}$ and $f_{vv} = \frac{\partial U_v}{\partial u}$ are the out-of-plane reaction forces in the horizontal and vertical ribbons, respectively. Therefore, the reaction forces (f_{yh} and f_{vv}) are not necessarily zero at the critical configuration, which is different from the aforementioned discussions. The other analyses are similar to that detailed in Section 2, and are not iterated herein.

Fig. 8b presents a contour plot of the stability coefficient E_r in terms of the position parameters (η_h and η_v), for fixed length ratio ($l_h/l_v = 1.5$) and width ratios ($\omega_h = 0.4$ and $\omega_v = 0.6$). The regime encased by the boundary curve of $E_r = 10^{-3}$ can yield reconfigurable 3D structures through the loading-path strategy, indicating that both the creases of the longer and shorter arms should be properly positioned. Five representative points in the design diagram were selected to carry out the assembly experiments, with use of 82% equal biaxial prestrain. The deformed configurations during sequential release appear in Fig. 8c, which show good agreements with the theoretical predictions. The results show that only the design point ('P2') with $E_r > 10^{-3}$ gives the pop-down configuration, while all of the others yield the pop-up configuration.

4.2. Cross-shaped patterns with locally stiffened elements

The above reconfigurable designs and those reported previously (Fu et al., 2018) mainly rely on the use of creases with reduced local stiffness to achieve the bistability of the structures. This section introduces a complementary strategy to realize bistable 3D structures, by incorporating stiffened segments with locally increased stiffness in the ribbon components. Fig. 8d shows a cross-shaped pattern consisting of such ribbon substructures, which is characterized by two geometric parameters, the factor (ω) of width increase and the normalized position parameter (η). The stability of this pattern can be analyzed using the same model developed in Section 2. The contour plot of the stability coefficient E_r in terms of the parameters (ω and η) are provided in Fig. 8e. Two isolated bistable domains exist, with one of them in the range of $0.2 < \eta < 0.45$ and the other in the range of $\eta > 0.85$. To achieve reconfigurable 3D structures using this design, the width ratio ω should be larger than 1.3 and the position parameter η should fall in the range of [0.20, 0.45] or [0.85, 1]. Three representative designs were selected to carry out the assembly experiments, with use of 82% equal biaxial prestrain. The deformed configurations after sequential release appear in Fig. 8f. The two designs with $E_r > 10^{-3}$ give the pop-down configurations and the other one yields the pop-up configuration, which is in agreement with the theoretical predictions. The design introduced herein can be extended to the structures with other multifold rotational symmetry, when the twisting deformations are not significant during the sequential loading. For example, for the designs with three-fold or six-fold rotational symmetry, FEA results demonstrate distinct bistable shapes during simultaneous and sequential releases, as shown in Figure S9 (Supplementary Information).

5. Conclusion

In summary, this paper presents a theoretical model to investigate the bistability of cross-shaped structures during the loading-path controlled 3D assembly. Three categories of cross-shaped patterns, either with a single crease or with the coexistence of two (or three) creases, are studied systematically, through combined theoretical modeling, numerical simulations and experimental measurements. Validated by the FEA and experiments, the developed model sheds light on the effects of various design parameters on the bistability of the structure. Based on the stability coefficient E_r proposed in this study, general design diagrams are constructed to evaluate the stability of pop-down configurations, for all of the three categories of cross-shaped patterns. The results suggest that the stability of pop-down configuration can be enhanced by introducing the α crease or properly positioned β crease. By contrast, the introduction of the γ crease always weakens its stability, and the weakening effect becomes stronger as the width ratio decreases. The design with coexistence of α and β creases yields the most stable pop-down configuration, as the largest stability coefficient is attained in all of the different cases studied herein. Furthermore, we demonstrate the extension of the developed model to other ribbon-shaped structures that do not involve twisting deformations during the assembly, such as the generalized crossed patterns and cross-shaped patterns with locally stiffened segments. These results provide theoretical guidelines for the design of reconfigurable 3D mesostructures and microelectronic devices for different targeted applications.

Acknowledgments

Y.Z. acknowledges support from the National Natural Science Foundation of China (# 11672152 and # 11722217), the Tsinghua National Laboratory for Information Science and Technology and the State Key Laboratory of Digital Manufacturing Equipment and Technology, Huazhong University of Science and Technology (# DMETKF2019005). H.F. acknowledges support from the National Natural Science Foundation of China (# 11602124), the Public Welfare Research Program of Jiaxing (# 2018AY32041) and the Open Foundation of IFET (# 2019KF1101).

References

- Ashwin, P., Creaser, J., Tsaneva-Atanasova, K., 2017. Fast and slow domino regimes in transient network dynamics. *Phys. Rev. E* 96, 052309.
- Babaee, S., Overvelde, J.T.B., Chen, E.R., Tournat, V., Bertoldi, K., 2016. Reconfigurable origami-inspired acoustic waveguides. *Sci. Adv.* 2, e1601019.
- Bian, J., Ding, Y., Duan, Y., Wan, X., Huang, Y., 2017. Buckling-driven self-assembly of self-similar inspired micro/nanofibers for ultra-stretchable electronics. *Soft Matter* 13, 7244–7254.
- Bolaños Quiñones, V., Zhu, H., Solovev, A., Mei, Y., Gracias, D.H., 2018. Origami biosystems: 3D assembly methods for biomedical applications. *Adv. Biosyst.* 2, 1800230.
- Budiansky, B., Hutchinson, J.W., 1966. A survey of some buckling problems. *AIAA J.* 4, 1505.
- Castle, T., 2014. Making the cut: lattice kirigami rules. *Phys. Rev. Lett.* 113, 245502.
- Castle, T., Sussman, D.M., Tanis, M., Kamien, R.D., 2016. Additive lattice kirigami. *Sci. Adv.* 2, e1601258.
- Chen, C., Tao, W., Su, Y., Wu, J., Song, J., 2013. Lateral buckling of interconnects in a noncoplanar mesh design for stretchable electronics. *J. Appl. Mech.-Trans. ASME* 80, 041031.
- Chen, Y., Liu, Y., Yan, Y., Zhi, Y., Chen, X., 2016a. Helical coil buckling mechanism for a stiff nanowire on an elastomeric substrate. *J. Mech. Phys. Solids* 95, 25–43.
- Chen, Y., Zhu, Y., Chen, X., Liu, Y., 2016b. Mechanism of the transition from in-plane buckling to helical buckling for a stiff nanowire on an elastomeric substrate. *J. Appl. Mech.-Trans. ASME* 83, 041011.
- Chen, Z., Chen, W., Song, J., 2017. Buckling of a stiff thin film on an elastic graded compliant substrate. In: Proceedings of the Royal Society A: Mathematical, Physical and Engineering Sciences, 473.
- Christ, S., Sonnenschein, B., Schimansky-Geier, L., 2017. Tristable and multiple bistable activity in complex random binary networks of two-state units. *Eur. Phys. J. B* 90, 14.
- Coleman, T.F., Li, Y.Y., 1996. An interior trust region approach for nonlinear minimization subject to bounds. *SIAM J. Optim.* 6, 418–445.
- Cui, I.X., Poblete, F.R., Zhu, Y., 2018. Origami/kirigami-guided morphing of composite sheets. *Adv. Funct. Mater.* 28, 7.
- Cui, J., Yao, S., Huang, Q., Adams, J.G.M., Zhu, Y., 2017. Controlling the self-folding of a polymer sheet using a local heater: the effect of the polymer-heater interface. *Soft Matter* 13, 3863–3870.
- Dias, M.A., Audoly, B., 2015. "Wunderlich, meet Kirchhoff": a general and unified description of elastic ribbons and thin rods. *J. Elast.* 119, 49–66.
- Dudte, L.H., Vouga, E., Tachi, T., Mahadevan, L., 2016. Programming curvature using origami tessellations. *Nat. Mater.* 15, 583–588.
- Fan, Z., Hwang, K.-C., Rogers, J.A., Huang, Y., Zhang, Y., 2018. A double perturbation method of postbuckling analysis in 2D curved beams for assembly of 3D ribbon-shaped structures. *J. Mech. Phys. Solids* 111, 215–238.
- Fan, Z., Wu, J., Ma, Q., Liu, Y., Su, Y., Hwang, K.-C., 2017. Post-buckling analysis of curved beams. *J. Appl. Mech.-Trans. ASME* 84, 031007.
- Felton, S., Tolley, M., Demaine, E., Rus, D., Wood, R., 2014. A method for building self-folding machines. *Science* 345, 644–646.
- Filipov, E.T., Paulino, G.H., Tachi, T., 2016. Origami tubes with reconfigurable polygonal cross-sections. In: Proceedings of the Royal Society A: Mathematical, Physical and Engineering Sciences, 472.
- Filipov, E.T., Tachi, T., Paulino, G.H., 2015. Origami tubes assembled into stiff, yet reconfigurable structures and metamaterials. In: Proceedings of the National Academy of Sciences of the United States of America, 112, pp. 12321–12326.
- Fu, C., Wang, T., Xu, F., Huo, Y., Potier-Ferry, M., 2019. A modeling and resolution framework for wrinkling in hyperelastic sheets at finite membrane strain. *J. Mech. Phys. Solids* 124, 446–470.
- Fu, H., Nan, K., Bai, W., Huang, W., Bai, K., Lu, L., Zhou, C., Liu, Y., Liu, F., Wang, J., Han, M., Yan, Z., Luan, H., Zhang, Y., Zhang, Y., Zhao, J., Cheng, X., Li, M., Lee, J.W., Liu, Y., Fang, D., Li, X., Huang, Y., Zhang, Y., Rogers, J.A., 2018. Morphable 3D mesostructures and microelectronic devices by multistable buckling mechanics. *Nat. Mater.* 17, 268–276.
- Gladman, A.S., Matsumoto, E.A., Nuzzo, R.G., Mahadevan, L., Lewis, J.A., 2016. Biomimetic 4D printing. *Nat. Mater.* 15, 413.
- Guo, X., Xu, Z., Zhang, F., Wang, X., Zi, Y., Rogers, J.A., Huang, Y., Zhang, Y., 2018. Reprogrammable 3D mesostructures through compressive buckling of thin films with prestrained shape memory polymer. *Acta Mech. Solida Sin.* 31, 589–598.
- Hu, W.Q., Lum, G.Z., Mastrangeli, M., Sitti, M., 2018. Small-scale soft-bodied robot with multimodal locomotion. *Nature* 554, 81–85.
- Hui, D., 1988. Postbuckling behavior of infinite beams on elastic foundations using koiter improved theory. *Int. J. Non Linear Mech.* 23, 113–123.
- Jeon, S.-J., Hauser, A.W., Hayward, R.C., 2017. Shape-Morphing materials from stimuli-responsive hydrogel hybrids. *Acc. Chem. Res.* 50, 161–169.
- Jiang, H., Sun, Y., Rogers, J.A., Huang, Y., 2007. Mechanics of precisely controlled thin film buckling on elastomeric substrate. *Appl. Phys. Lett.* 90, 133119.
- Jiang, H., Sun, Y., Rogers, J.A., Huang, Y., 2008. Post-buckling analysis for the precisely controlled buckling of thin film encapsulated by elastomeric substrates. *Int. J. Solids Struct.* 45, 2014–2023.
- Jiao, P., Borchani, W., Lajnef, N., 2017. Large deformation solutions to post-buckled beams confined by movable and flexible constraints: a static and dynamic analysis. *Int. J. Solids Struct.* 128, 85–98.
- Lacarbonara, W., 2008. Buckling and post-buckling of non-uniform non-linearly elastic rods. *Int. J. Mech. Sci.* 50, 1316–1325.
- Li, R., Li, M., Su, Y., Song, J., Ni, X., 2013. An analytical mechanics model for the island-bridge structure of stretchable electronics. *Soft Matter* 9, 8476–8482.
- Li, Y., Chen, C., Fang, B., Zhang, J., Song, J., 2012. Postbuckling of piezoelectric nanobeams with surface effects. *Int. J. Appl. Mech.* 4, 1250018.
- Liu, F., Chen, Y., Song, H., Zhang, F., Fan, Z., Liu, Y., Feng, X., Rogers, J.A., Huang, Y., Zhang, Y., 2019. High Performance, tunable electrically small antennas through mechanically guided 3D assembly. *Small* 15, 1804055.
- Liu, L., Lu, N., 2016. Variational formulations, instabilities and critical loadings of space curved beams. *Int. J. Solids Struct.* 87, 48–60.
- Liu, Y., Yan, Z., Lin, Q., Guo, X., Han, M., Nan, K., Hwang, K.-C., Huang, Y., Zhang, Y., Rogers, J.A., 2016. Guided formation of 3D helical mesostructures by mechanical buckling: analytical modeling and experimental validation. *Adv. Funct. Mater.* 26, 2909–2918.
- Lv, C., Krishnaraju, D., Konjevod, G., Yu, H.Y., Jiang, H.Q., 2014. Origami based mechanical metamaterials. *Sci. Rep.* 4, 5979.
- Ma, Q., Cheng, H., Jang, K.-I., Luan, H., Hwang, K.-C., Rogers, J.A., Huang, Y., Zhang, Y., 2016. A nonlinear mechanics model of bio-inspired hierarchical lattice materials consisting of horseshoe microstructures. *J. Mech. Phys. Solids* 90, 179–202.
- Miller, J.T., Su, T., Duscan, E.B.V., Pabon, J., Wicks, N., Bertoldi, K., Reis, P.M., 2015. Buckling-induced lock-up of a slender rod injected into a horizontal cylinder. *Int. J. Solids Struct.* 72, 153–164.
- Ni, Y., Soh, A.K., 2014. On the growth of buckle-delamination pattern in compressed anisotropic thin films. *Acta Mater.* 69, 37–46.
- Ou, J.Y., Plum, E., Zhang, J.F., Zheludev, N.I., 2013. An electromechanically reconfigurable plasmonic metamaterial operating in the near-infrared. *Nat. Nanotechnol.* 8, 252–255.
- Overvelde, J.T.B., 2016. A three-dimensional actuated origami-inspired transformable metamaterial with multiple degrees of freedom. *Nat. Commun.* 7, 10929.
- Pan, K., Ni, Y., He, L., Huang, R., 2014. Nonlinear analysis of compressed elastic thin films on elastic substrates: from wrinkling to buckle-delamination. *Int. J. Solids Struct.* 51, 3715–3726.
- Pan, T., Pharr, M., Ma, Y., Ning, R., Yan, Z., Xu, R., Feng, X., Huang, Y., Rogers, J.A., 2017. Experimental and theoretical studies of serpentine interconnects on ultrathin elastomers for stretchable electronics. *Adv. Funct. Mater.* 27, 1702589.
- Reis, P.M., 2015. A perspective on the revival of structural (In) stability with novel opportunities for function: from buckiphobia to buckiphilia. *J. Appl. Mech.-Trans. ASME* 82, 111001.
- Rogers, J., Huang, Y.G., Schmidt, O.G., Gracias, D.H., 2016. Origami MEMS and NEMS. *MRS Bull.* 41.
- Schenk, M., Guest, S.D., 2013. Geometry of miura-folded metamaterials. In: Proceedings of the National Academy of Sciences of the United States of America, 110, pp. 3276–3281.

- Shim, T.S., Kim, S.H., Heo, C.J., Jeon, H.C., Yang, S.M., 2012. Controlled origami folding of hydrogel bilayers with sustained reversibility for robust microcarriers. *Angew. Chem. Int. Edit.* 51, 1420–1423.
- Silverberg, J.L., 2014. Using origami design principles to fold reprogrammable mechanical metamaterials. *Science* 345, 647–650.
- Song, J., Huang, Y., Xiao, J., Wang, S., Hwang, K.C., Ko, H.C., Kim, D.H., Stoykovich, M.P., Rogers, J.A., 2009. Mechanics of noncoplanar mesh design for stretchable electronic circuits. *J. Appl. Phys.* 105, 123516.
- Stu, Y., Wu, J., Fan, Z., Hwang, K.-C., Song, J., Huang, Y., Rogers, J.A., 2012. Postbuckling analysis and its application to stretchable electronics. *J. Mech. Phys. Solids* 60, 487–508.
- Sussman, D.M., 2015. Algorithmic lattice kirigami: a route to pluripotent materials. In: Proceedings of the National Academy of Sciences of the United States of America, 112, pp. 7449–7453.
- Wagner, T.J.W., Vella, D., 2013. The 'Sticky Elastica': delamination blisters beyond small deformations. *Soft Matter* 9, 1025–1030.
- Wang, A., Avila, R., Ma, Y., 2017. Mechanics design for buckling of thin ribbons on an elastomeric substrate without material failure. *J. Appl. Mech.* 84, 094501.
- Wang, X., Guo, X., Ye, J., Zheng, N., Kohli, P., Choi, D., Zhang, Y., Xie, Z., Zhang, Q., Luan, H., Nan, K., Kim, B.H., Xu, Y., Shan, X., Bai, W., Sun, R., Wang, Z., Jang, H., Zhang, F., Ma, Y., Xu, Z., Feng, X., Xie, T., Huang, Y., Zhang, Y., & Rogers, J.A. 2019. Freestanding 3D mesostructures, functional devices, and shape-programmable systems based on mechanically induced assembly with shape memory polymers. *Adv. Mater.* 31, 1805615.
- Wang, Z., Ruimi, A., Srinivasa, A.R., 2015. A direct minimization technique for finding minimum energy configurations for beam buckling and post-buckling problems with constraints. *Int. J. Solids Struct.* 72, 165–173.
- Widlund, T., Yang, S., Hsu, Y.-Y., Lu, N., 2014. Stretchability and compliance of freestanding serpentine-shaped ribbons. *Int. J. Solids Struct.* 51, 4026–4037.
- Xu, F., Potier-Ferry, M., 2016. A multi-scale modeling framework for instabilities of film/substrate systems. *J. Mech. Phys. Solids* 86, 150–172.
- Xu, S., Yan, Z., Jang, K.-I., Huang, W., Fu, H., Kim, J., Wei, Z., Flavin, M., McCracken, J., Wang, R., Badea, A., Liu, Y., Xiao, D., Zhou, G., Lee, J., Chung, H.U., Cheng, H., Ren, W., Banks, A., Li, X., Paik, U., Nuzzo, R.G., Huang, Y., Zhang, Y., Rogers, J.A., 2015. Assembly of micro/nanomaterials into complex, three-dimensional architectures by compressive buckling. *Science* 347, 154–159.
- Yan, Z., 2016. Controlled mechanical buckling for origami-inspired construction of 3D microstructures in advanced materials. *Adv. Funct. Mater.* 26, 2629–2639.
- Yang, N., Silverberg, J.L., 2017. Decoupling local mechanics from large-scale structure in modular metamaterials. In: Proceedings of the National Academy of Sciences of the United States of America, 114, pp. 3590–3595.
- Yang, S., Qiao, S., Lu, N., 2016. Elasticity solutions to nonbuckling serpentine ribbons. *J. Appl. Mech.* 84, 021004.
- Zhang, F., Fan, Z., Zhang, Y., 2018a. A theoretical model of postbuckling in straight ribbons with engineered thickness distributions for three-dimensional assembly. *Int. J. Solids Struct.* 147, 254–271.
- Zhang, H., Guo, X., Wu, J., Fang, D., & Zhang, Y. (2018b). Soft mechanical metamaterials with unusual swelling behavior and tunable stress-strain curves. *Science Advances* 4, eaar8535.
- Zhang, Q., Wommer, J., O'Rourke, C., Teitelman, J., Tang, Y., Robison, J., Lin, G., Yin, J., 2017a. Origami and kirigami inspired self-folding for programming three-dimensional shape shifting of polymer sheets with light. *Extreme Mech. Lett.* 11, 111–120.
- Zhang, Y., Huang, Y., Rogers, J.A., 2015. Mechanics of stretchable batteries and supercapacitors. *Curr. Opin. Solid State Mater. Sci.* 19, 190–199.
- Zhang, Y., Zhang, F., Yan, Z., Ma, Q., Li, X., Huang, Y., Rogers, J.A., 2017b. Printing, folding and assembly methods for forming 3D mesostructures in advanced materials. *Nat. Rev. Mater.* 2, 17019.
- Zhang, Y.H., 2015. A mechanically driven form of kirigami as a route to 3D mesostructures in micro/nanomembranes. In: Proceedings of the National Academy of Sciences of the United States of America, 112, pp. 11757–11764.